Published in final edited form as:
Opt Express. 2009 March 30; 17(7): 5125–5138.

Effects of sampling strategy on image quality in noncontact panoramic fluorescence diffuse optical tomography for small animal imaging

Xiaofeng Zhang* and **Cristian Badea**
Department of Radiology, Center for In Vivo Microscopy, Duke University Medical Center, Durham, NC, 27710, USA

Abstract

Fluorescence diffuse optical tomography is an emerging technology for molecular imaging with recent technological advances in biomarkers and photonics. The introduction of noncontact imaging methods enables very large-scale data acquisition that is orders of magnitude larger than that from earlier systems. In this study, the effects of sampling strategy on image quality were investigated using an imaging phantom mimicking small animals and further analyzed using singular value analysis. The sampling strategy was represented in terms of a number of key acquisition parameters, namely the numbers of sources, detectors, and imaging angles. A number of metrics were defined to quantitatively evaluate image quality. The effects of acquisition parameters on image quality were subsequently studied by varying each of the parameters within a reasonable range while maintaining the other parameters constant, a method analogue to partial derivative in mathematical analysis. Image quality improves at a much slower rate if the acquisition parameters are above certain critical values (~5 sources, ~15 detectors, and ~20 angles for our system). These critical values remain virtually the same even if other acquisition parameters are doubled. It is also found that increasing different acquisition parameters improves image quality with different efficiencies in terms of the number of measurements: for a system characterized by a smaller threshold in singular value analysis (less than 10^{-5} in our study), the number of sources is the most efficient, followed by the number of detectors and subsequently the number of imaging angles; however, for systems characterized by a larger threshold, the numbers of sources and angles are equally more efficient than the number of detectors.

1. Introduction

Fluorescence diffuse optical tomography (FDOT) in small animals is currently an active field of research with promises for applications to basic science and medicine. This is because this technology offers a potentially revolutionary means to noninvasive *in vivo* tomographic imaging with unmatched sensitivity and molecular specificity for medical and preclinical imaging, particularly in cancer studies [1–3].

In parallel with engineering advances in fluorescent probes that selectively bind to various molecular targets, as reviewed in [4,5], researchers are also developing better imaging apparatus and methods for FDOT to provide tomographic mapping of biomarker-driven

*Corresponding author: E-mail: steve.zhang@duke.edu.

OCIS codes: (170.3880) Medical and biological imaging; (110.3000) Image quality assessment; (110.6880) Three-dimensional image acquisition; (110.6960) Tomography

distributions of these probes, e.g., [6–12]. Compared to other leading biomedical imaging modalities, such as x-ray computed tomography (CT) and magnetic resonance imaging (MRI), achieving high-quality FDOT images is a challenging task mostly due to the diffuse nature of light propagation in tissue [13,14]. Nonetheless, image quality can be improved from multiple aspects such as advanced imaging apparatus, accurate photon migration models, sound sampling strategy, and sophisticated reconstruction algorithms.

Rapid advances in photonics have greatly improved the variety and performance of available instruments for FDOT, particularly laser diodes and charge-coupled devices (CCD). In terms of system configuration, many FDOT systems for small animals use optical fibers to couple light to and/or from the skin of the animal, e.g. [15,16]. As a result, these system configurations typically lead to an underdetermined image reconstruction problem and are difficult to extend to large-scale data acquisition because of the physical constraints posed by optical fibers. These limitations can be eliminated by using noncontact acquisition techniques: a scanning laser as the light source and a CCD camera as the optical sensor [4,6,9,16,17]. A recent publication has shown that noncontact techniques produce better imaging results compared to fiber-based methods [18]. In many small animal FDOT systems, imaging chambers filled with optical matching fluid are used. In fiber-based systems, the main purpose of the imaging chamber is to achieve proper optical contact; and in noncontact systems, computation can be significantly simplified by using slab geometry due to optical matching, e.g., [4,16]. However, the imaging chamber makes it very difficult to achieve panoramic data acquisition for *in vivo* studies, which is critical to depth-resolution in FDOT. Studies show that FDOT could be performed without the imaging chamber, e.g., [6,19,20]. With a fully noncontact and fluid-free method, a rotation stage can be integrated to enable panoramic data acquisition on a vertically positioned animal, as reported recently by Deliolanis et al. in [19].

The introduction of a fully noncontact imaging system is clearly an exciting advancement in FDOT hardware development because it allows dramatically increased sampling density as well as unprecedented flexibility in data sampling strategy compared to fiber-based systems. With the typical number of pixels available on a modern CCD camera ($\sim 10^6$), a reasonable laser scanning density ($\sim 10^2$–10^4 points within an area of ~25×25 mm), and the number of angles a rotation stage can provide ($\sim 10^2$), a noncontact FDOT system can potentially provide 10^{10}–10^{12} measurements. Using this approach, the reconstruction problem in FDOT can easily become overdetermined, given that the usual upper limit of field-of-view in small animal imaging (30×30×60 mm) contains only 5.4×10^4 of 1 mm^3 voxels, a typical resolution limit due to scattering in tissue. Furthermore, with a scanning laser and a CCD camera, the points of illumination and sensing can be virtually anywhere on the skin of the animal. Such flexibility in sampling inevitably raises the interesting question – what would be the optimal data sampling strategy in order to achieve the best image quality with the least amount of sampling? Extensive studies regarding different imaging strategies have been conducted for FDOT and diffuse optical tomography (DOT), which share similar physical and mathematical models, as discussed in [21–26]. Nonetheless, the majority of these studies were performed in the context of imaging in humans or using fiber-based systems. Studies for noncontact FDOT in small animal imaging are still scarce in the literature. One such study on the optimal sampling geometry for the FDOT was recently reported by Lasser et al. [27], in which an analytical model based on the diffusion approximation was used to compute the forward problem and singular value analysis (SVA) based on a previously determined threshold was used to optimize source and detector arrangements and the field-of-view (FOV). The sampling strategies determined by SVA were experimentally verified using an imaging phantom.

In this study, we investigate the effects of different sampling strategies on image quality using a different approach and extend the number of parameters under investigation. Specifically, three acquisition parameters that are fundamental to experimental designs were chosen for this

study: the number of source positions, the number of detector positions, and the number of imaging angles. The number of source positions is linearly related to the acquisition time in scanning- or switching-source systems. The number of detector positions becomes less a hardware limit in a noncontact optical imaging system due to the relatively large number of pixels available in a CCD camera. Nonetheless, it is still a major limiting factor for the rate of data acquisition. The number of imaging angles is linearly related to data acquisition time as well. All of these acquisition parameters contribute linearly to the matrix size in image reconstruction. We first constructed a noncontact liquid-free panoramic FDOT system and performed experiments on an imaging phantom. A number of metrics of image quality were adopted to quantitatively evaluate the effects of these acquisition parameters on imaging results. Based on our experimental configuration, SVA was used to evaluate the overall performance of the imaging system in terms of the number of singular values (NSV) above a series of different thresholds to interpret and generalize our experimental results.

2. Methods

2.1. Hardware configuration and experimental design

Our FDOT system adopts the same architecture as reported in [19]. The optical sensor is an intensified CCD (ICCD) camera (PicoStar HRI, LaVision, Germany), which has a 2-D array of 1370×1040 pixels with 12-bit digitization. The light source is a 785 nm continuous-wave (CW) laser diode (HL7851G, Hitachi, Japan), which is thermally and electrically stabilized (LDC205C, TED200C, and TCLDM9, Thorlabs, Germany) and coupled to the surface of a lab-built imaging phantom via a galvo-scanner, i.e., a dual-axis galvanometer equipped with a pair of high-reflectance mirrors (6230H, Cambridge Technology, MA). The imaging phantom is vertically positioned on a motorized rotation stage (Oriel 13049, Newport, CA). The system configuration is schematically shown in Fig. 1(a) and (b). A filter wheel was used to switch between the excitation and emission band-pass filters (785 and 830 nm central wavelengths, respectively, and 10 nm pass-band).

The imaging phantom used in this study was constructed as a cylinder (Nylon 6/6) with 23 mm outer diameter (1 mm wall thickness) and filled with approximately 1% v/v fat emulsion (diluted from 10% Intralipid, Fresenius Kabi, Sweden) and India ink (off the shelf) in deionized water to simulate the optical properties of small animals. The phantom enclosed two thin-wall glass tubes (3 and 4 mm outer diameter, 0.3 and 0.4 mm wall thickness, respectively, NMR tubes by Wilmad LabGlass, NJ) both filled with 10 μM indocyanine green (ICG or Cardiogreen, Sigma-Aldrich, MO) aqueous solution (deionized water), see Fig. 1(c). The optical properties of the components of the imaging phantom were listed in Table 1. The absorption and scattering coefficients were measured at 785 nm, and the indices of refraction were taken from typical values in the literature.

The laser and the camera were arranged in a transillumination configuration—180° apart from each other with respect to the imaging phantom. The galvo-scanner moves the laser beam horizontally across the surface of the phantom in small steps at a constant angular interval and thus creates a discrete 1-D pattern of light source positions perpendicular to the symmetric axis of the cylinder, as illustrated in Fig. 1(b) and (c). For each source position, the ICCD camera was triggered (20 ms exposure time) to take a fluorescence image (at the emission wavelength, using the 830 nm filter), in which a series of points were chosen in 1-D (at the same height as the source positions) as the detector positions. For each detector position, its signal intensity was an average over a small cluster of pixels (5×5 in this study) around it to increase the signal-to-noise ratio (SNR), which corresponds to an area of 0.3×0.3 mm on the projected 2-D surface of the imaging phantom. After the galvo-scanner completes a scan and resumes its initial state, the imaging phantom was turned a small angle by the rotation stage, followed by another laser scan by the galvo-scanner. This process repeats until the phantom returns to its initial angular

position. Afterwards, the above imaging procedure was repeated at the excitation wavelength (785 nm) to obtain the distribution of excitation light in order to normalize the previously acquired fluorescence signal [10]. In this study, a total of 21 source positions, 30 detector positions, and 180 imaging angles were used during data acquisition, after which subsets of this full dataset were selected for each of the study cases (described later) to ensure consistent experimental conditions. The source positions spanned an arc of 100°; and the detector positions covered 140°on the cylindrical surface of the phantom, both of which had approximately the same angular sampling density of 5°/sample on the surface of the imaging phantom. In each subset, the sources, detectors, and imaging angles were evenly distributed (rounded to the nearest available sampling points) in the full dataset. The triggering of the ICCD camera and the actuation of the rotation stage were controlled using our lab-developed LabVIEW (v8.5, National Instruments, TX) applications and auxiliary computer hardware.

Due to the large number of possible combinations of the acquisition parameters, an exhaustive case study is impractical. We adopted an analyzing method analogue to partial derivative in mathematical analysis: only one parameter is variable at a time while maintaining the other two constant. In this study, image quality is analyzed for the following 9 cases, as listed in Table 2: Case (1), variable number of sources and fixed numbers of detectors and imaging angles; Case (2), repeat Case (1) but double the number of detectors; Case (3), repeat Case (1) but double the number of angles; Cases (4)–(6), variable number of detectors and double the numbers of sources and angles, respectively; Cases (7)–(9), variable number of imaging angles and double the numbers of sources and detectors, respectively. The values of the constant parameters used in Cases (1), (4), and (7) give reasonably good image quality, which were chosen empirically based on initial trail experiments.

2.2. Forward problem and image reconstruction

The forward problem of FDOT was based on the Born approximation of the diffusion equation, similar to the normalized Born method proposed by Ntziachristos and Weissleder in [10]. Fluorescence was modeled as a linear equation $AX = b$, where the measured fluorescence b is a vector linearly related to the 3-D fluorophore distribution X via a sensitivity matrix A. The fluorescence (optical signal measured at the emission wavelength) was normalized by the signal at the excitation wavelength under otherwise identical experimental conditions; the normalized sensitivity matrix was computed using a Monte Carlo (MC) simulation-based method developed by Zhang et al. [28].

In MC simulations, the imaging medium was modeled to precisely represent our imaging phantom as a two-layered cylinder: a homogeneous cylindrical scattering material (a liquid mixture of Intralipid and India ink) enclosed by a thin layer of homogeneous material of different optical properties (Nylon 6/6). 90 millions of photons were used in the simulations. The voxel size of the discretized imaging medium was $(0.1\ \text{mm})^3$ in MC simulations and was down-sampled to $(1\ \text{mm})^3$ while computing the sensitivity matrix. The exact geometry and optical properties of the imaging phantom were set to match our experimental conditions previously described in detail in section *Hardware configuration and experimental design.* The exact positions of the sources and the detectors were obtained by geometrical calculation. The orientations of the light sources (the incident angle of the laser) and the optical detectors (the principle escaping angle of the fluorescent light) in the simulations are parallel to the axis on which the galvo-scanner, the imaging phantom, and the camera are positioned. This parallel configuration in MC simulations effectively avoids the type of distortion of signal intensity due to geometrical effects arising from the curved surface when the sources and detectors are modeled as being perpendicular to the surface of the phantom (as is the case in typical fiber-based systems), which has to be corrected, for example, using the methods described by Schulz et al. in [29]. Second-order geometrical distortion due to the lens and the scanning laser are

ignored due to the relatively large distance from the phantom to the lens (~240 mm) and to the galvo-scanner (~200 mm) compared to the representative size of the imaging phantom (~20 mm).

Image reconstruction was performed on the normalized Born equation to resolve the fluorophore distribution in 3-D, using a conjugate gradient-based iterative method. Starting from an all-zero initial guess, the algorithm iteratively updates the solution according to the conjugate gradient method [30] until the value of the cost function H is less than a predetermined limit of 10^{-6}. This cost function was defined as a weighted sum of three penalty terms: square of L-2 norm of the residual error, image intensity, and its gradient

$$H(X)=\|\mathrm{AX}-b\|_2^2+\alpha\int_\Omega\|X\|_2^2\,\mathrm{dr}+\beta\int_\Omega\|\nabla X\|_2^2\,\mathrm{dr} \quad (1)$$

where $\|k\|_2$ is the *L-2* norm of vector k, Ω is the region of interest, and r is position. Using this definition for the cost function, the reconstructed image is a regularized result of image fidelity, sparsity, and smoothness, respectively. The optimal regularization parameters α and β were determined by inspection (10^{-3} and 10^{-4}, respectively) and were maintained the same throughout this study.

As a result of the relatively long data acquisition time (~45 minutes for each 360° acquisition consisting of 21 source positions and 180 imaging angles with 0.5 and 4 s delays between consecutive laser scanning positions and phantom rotations, respectively) and the relatively high energy density of the laser (~50 mW/mm^2 at the surface of the phantom), the effect of photo-bleaching [31] on signal intensity has to be taken into account in image reconstruction: a fluorescence image taken immediately after regular data acquisition (i.e., the 181st image at the emission wavelength) produced an average intensity of about 40% less than the 1st image at all the detector positions. This effect was corrected for each measurement by modeling photo-bleaching as a global effect on the entire imaging phantom using the following formula:

$$p_{m,n}(i)=p_{m,n}(0)\left[p_{m,n}(N)/p_{m,n}(0)\right]^{i/N}=p_{m,n}(0)^{1-i/N}\,p_{m,n}(N)^{i/N} \quad (2)$$

where $p_{m,n}(i)$ is the fractional signal intensity measured for the m-th source and the n-th detector at the i-th imaging angle ($0 \le i \le N$), and N is the total number of imaging angles. It is worth noting that the index of imaging angle was used to model photo-bleaching instead of using the exposure time of the fluorophore to the laser because the laser was scanning at a constant time interval. The effect of photo-bleaching on measurements at the excitation wavelength was ignored because of the relatively small fraction of absorption by the fluorophore at this wavelength compared to its surrounding medium in the imaging phantom.

The raw images produced by the image reconstruction algorithm had a matrix size of 23×23×15 with a voxel size of (1 mm)^3. They were further processed for later quantitative analysis: in a raw 3-D image, only the center slice where the sources and detectors were located was retained due to the symmetry of light propagation about this plane; the background noise was removed using a threshold such that only two disconnected features remain; and furthermore, the reconstructed fluorescent structures were defined as the clusters of pixels having values greater than half of the local maxima. This image processing procedure was programmed using MATLAB (R2008a, The MathWork, MA) and applied to all raw reconstructed images without further human intervention. It is worth noting that although the particular choice of the image processing method is less than ideal and that it has incorporated prior information (we assumed that two distinct fluorescent structures exist as a prior), which is not generally available in typical biomedical imaging, the use of this automated procedure greatly reduces the

dependence of the reconstruction results on a particular operator and thus makes image quality comparison at the later stage more objective.

2.3 Image quality metrics and singular value analysis

The definition of image quality is a key to its evaluation. From a theoretical point of view, in the context of biomedical imaging the reconstructed image should truthfully represent the actual shape of the internal structures under investigation, correctly localize the structures, and also accurately reconstruct intensities of different structures. In accordance with these criteria, image quality was defined in terms of the following metrics: root mean square (RMS) error, localization error, and relative intensity. The RMS error describes the global difference between the reconstructed and the true images

$$\text{RMS error}=\left\{\sum_{i=1}^{N}(x_i - x_{0,i})^2/N\right\}^{1/2} \tag{3}$$

where x_i and $x_{0,i}$ are the i-th elements in the reconstructed and the true images respectively, and N is the total number of voxels within the FOV. The localization error was defined as the displacement of the centroid of the smaller fluorescent structure in the reconstructed image from its true location. The relative intensity was defined as the ratio of the average intensities of the two reconstructed structures, which is particularly relevant in FDOT because it is an indicator of imaging artifact arising from the spatially variant sensitivity function associated with diffuse optical imaging [17,32,33].

From a practical point of view, the efficiency of measurements is another important factor in biomedical imaging because of the constraints in time and resources due to various reasons. In this study, the measurement efficiency is quantified by plotting the values of image quality metrics against the total number of measurements. The number of measurements dictates the required imaging and computing resources, which in most cases are the limiting factors for high-resolution or high-speed imaging.

SVA was used to interpret the overall performance of the FDOT system in terms of the number of truncated singular values, which represents the number of usable modes in the measurement space that can be mapped onto the image space given by singular value decomposition. More detailed descriptions on SVA in the context of diffuse optical imaging were given in [27,34]. Specifically, the normalized sensitivity matrix underwent singular value decomposition (SVD) using built-in routines in MATLAB. The resulting vector of singular values was normalized by its largest element. The normalized vector of singular values was then truncated at a series of thresholds (10^{-3}, 10^{-4}, 10^{-5}, 10^{-6}, and 10^{-7}) respectively. Subsequently, the remaining numbers of singular values after truncation were plotted against different acquisition parameters (numbers of sources, detectors, and imaging angles) and the total number of measurements, i.e., the product of the acquisition parameters, respectively.

3. Results and Discussion

3.1. Experimental data

Representative reconstruction results from different number of sources (from 1 to 20) and different number of detectors (from 2 to 10) with fixed 16 imaging angles are shown in Fig. 2. Image quality shows strong dependence (by visual inspection) on the acquisition parameters (variable numbers of sources and detectors, with a fixed number of imaging angles). Fig. 2 also clearly demonstrates that image quality improves in general with increased acquisition parameters; and that abnormalities (“exceptions”) exist when the numbers of source and

detectors are small, as shown in the lower-left quadrant of Fig. 2. Such abnormality in image quality can mislead towards false interpretations of the images.

In Fig. 3, image quality metrics are plotted against the number of sources, the number of detectors, and the number of imaging angles (from left to right) for the study cases listed in Table 2. For RMS and localization errors, as shown in Figs. 3(a) and (b), respectively, a smaller value indicates better image quality. For relative intensity, shown in Fig. 3(c), however, a value closer to unity represents better image quality. In these plots, the curves of image quality metrics either monotonically improve or severely oscillate before they eventually stabilize to a certain level. Although the total number of measurements can differ significantly in different cases, for example, comparing Case 1 with Case 2 or 3, the values of all image quality metrics stabilize after the acquisition parameters are greater than certain critical values: ~5 for the number of sources, ~15 for detectors, and ~20 for imaging angles, as marked by broken lines in Figs. 3 (a)–(c). Noted that these critical values remain virtually the same even though other parameters have changed, as shown in Fig. 3(a1) in particular. This might seem to contradict the conventional belief that more measurement would result in better image quality. In fact, as further proven using SVA, this phenomenon reflects the differences in measurement efficiencies of different acquisition parameters.

To better illustrate the differences in measurement efficiency, the same image quality metrics are plotted against the total number of measurements, which is the product of the numbers of sources, detectors, and angles, for all study cases, as shown in Figs. 3(d)–(f). We define the criteria of finding higher measurement efficiency for different acquisition parameters as "obtaining the same image quality with a smaller number of measurements," or equivalently as "obtaining a better image quality with the same number of measurements." Using these criteria, Fig. 3(d1) suggests that the increase in the number of sources is the most efficient way to lower RMS errors. Indeed, doubling either the number of detectors or angles does not reduce RMS error, although the number of measurements has been doubled for the same number of sources (Cases 2 and 3 compared to Case 1). From Fig. 3(d2), one can draw the conclusion that increasing the number of sources is more efficient that the number of detectors, which is subsequently more efficient than the number of angles, because for the same number of measurements, doubling the number of sources (Case 5) gives a smaller RMS error, while doubling the number of angles (Case 6) results in a larger RMS error. Fig. 3(d3) shows that doubling the number of sources (Case 8) reduces the RMS error. Overall, Fig. 3(d) consistently demonstrate that for our experimental configuration and reasonably close to the chosen values of acquisition parameters, increasing the number of sources is more efficient than the number of detectors, which is in turn is more efficient than increasing the number of imaging angles. The same conclusion can be drawn using the localization error and relative intensity, as shown in Figs. 3(e) and (f), respectively. It is relatively less definitive to use localization error to determine the order of efficiency because its stabilized value reaches sub-millimeter levels, which are less than the voxel size in image reconstruction, and thus makes comparison relatively difficult.

3.2. Singular value analysis

The SVA results for different sampling strategies (Cases 1–9 listed in Table 2) are shown in Fig. 4. In the top row, the NSV above a series of thresholds (10^{-3}, 10^{-4}, till 10^{-7}) are plotted against the number of sources, the number of detectors, and the number of imaging angles, as shown in Figs. 4(a), which corresponds to Cases 1, 4, and 7, respectively. In these plots, the behavior of each curve is noticeably different from each other with respect to different acquisition parameters: the amplitudes that the curves reach and their linearity, for example. The difference is more prominent when the threshold is relatively small (starting from 10^{-5}, but 10^{-6} and 10^{-7} in particular).

We compared the critical values observed from the experimental data and SVA, at which the improvement of image quality and the increment rate of the NSV curves change significantly, and found that the threshold of 10^{-5} in SVA best characterize our experimental data, as shown in Fig. 4(b). In each of these plots, a NSV curve initially increases rapidly and eventually reaches a plateau. The transition between these two stages is the "critical value" of the corresponding acquisition parameter in our FDOT system because it is around this point when the increment rate of NSV starts to decrease dramatically. It is interesting to notice the similarity between the NSV curves with different acquisition constants, i.e., comparing curves for Cases 1 through 3, 4 through 6, and 7 through 9. The critical values remain virtually the same even though other constant parameters have been doubled—the same conclusion drawn from the experimental data (~5 sources, ~15 detectors, and ~20 angles, as marked by broken lines in Fig. 3). The shapes of the NSV curves are also consistent with our experimental results. For example, the transition of the NSV curves using variable number of detectors is more gradual than those of the other two parameters (Fig. 4[b2] compared to [b1] and [b3]), which results in less significant changes in image quality (from experimental data) before and after the critical values with variable number of detectors then the other two acquisition parameters (Fig. 3[a2]–[c2] compared to [a1]–[c1] and [a3]–[c3]). As expected, when the constant acquisition parameters were doubled, the NSV curves (green and blue) are in general higher than the original curves (red).

When the NSV are plotted against the number of measurements, the red curve can be on top of, in between, or beneath the green and blue curves, as shown in Fig. 4(c), which clearly indicates the relative measurement efficiencies of different acquisition parameters. More specifically, because doubling the number of detectors and angles does not increase the NSV for variable number of sources, as shown in Fig. 4(c1); because doubling the number of sources increases the NSV, while doubling the number of angles not, for variable number of detectors, Fig. 4(c2); and because doubling the number of sources and detectors both increase the NSV for variable number of angles, Fig. 4(c3), it can be concluded that with a threshold of 10^{-5}, increasing the number of sources is more efficient in improving NSV than the number of detectors, which in turn is more efficient than the number of angles. This conclusion is identical to the one drawn from our experimental data. We note that an increase in the NSV is always desirable.

However, if using a larger threshold, e.g., 10^{-4}, the relative order of measurement efficiency changes to: increasing the numbers of sources or angles is equally more efficient than the number of detectors, as shown in Fig. 4(d). Using a threshold of 10^{-3} gives the same result (data not shown). Using a smaller threshold, e.g. 10^{-6} (Fig. 4(e)) and 10^{-7} (data not shown), the relative efficiencies of acquisition parameters are the same as using the threshold of 10^{-5}, except that the differences between the acquisition parameters are less significant and the overall trend of the NSV curves resembles closer to a straight line, which occurs when the threshold is zero.

In this study, the overall performance of our FDOT system was characterized by a threshold of 10^{-5} used in SVA. The effect of sampling strategies on image quality was compared in terms of a number of image quality metrics for reconstruction results and in terms of the NSV in a more generalized SVA. The results are representative for similar noncontact FDOT systems, such as [19], and can be used to assist the choice of acquisition parameters in experimental designs—a tradeoff between image quality and resources.

The NSV curves are in general consistent with the image quality metrics defined in this study. Nonetheless, a larger NSV does not necessarily translate into a higher score in every metric. This is because a particular image quality metric represents only one figure of merit of a complex imaging system, which consists of imaging apparatus and reconstruction methods.

On the other hand, differences due to specific imaging hardware, experimental configurations, and reconstruction methods can alter the outcome of the analysis. Nonetheless, this study adopted a way to characterize the overall performance of an imaging system in terms of the threshold in SVA. With the same imaging apparatus and similar experimental configurations, this threshold can be used to predict outcomes of FDOT imaging using other sampling strategies. With this method, a more generalized analysis of sampling strategies can be conducted with more acquisition parameters, for example, the 2-D distribution of sampling points for sources and detectors, as well as angular coverage and distribution of imaging angles. The effect of experimental configuration, e.g., relative angular positions of the scanning laser and the camera, on the characteristic SVA threshold and further on image quality can be investigated using this approach as well, which is beyond the scope of this study.

It is important to point out that this study has been purposefully limited to 2-D on a limited imaging parameters, although indeed FDOT is fundamentally a 3-D imaging method. This is primarily because the image quality is affected by so many parameters that it would be impractical to cover the full effects of all possible imaging parameters and experimental configurations. Instead, we are focusing only on the most fundamental imaging parameters that are pertinent to the majority of FDOT experiments. For the same reason, the phantom design and image analysis were limited to 2-D as well in order to avoid being too specific on particular image processing algorithms and to avoid the complexity of image analysis in 3-D.

4. Conclusions

We found that critical values for acquisition parameters exist, beyond which image quality improves at a much slower rate. These critical values largely remain the same despite significant change of other acquisition parameters. In terms of the number of measurements, increasing the number of sources is more efficient in improving image quality than the number of detectors and subsequently the number of angles, if the SVA threshold is small (less than or equal to 10^{-5} using our imaging system); or the number of sources and the number of imaging angles are almost equally more efficient than the number of detectors, if the SVA threshold is large (greater or equal to 10^{-4} in our study). Based on this study, we believe a generalized optimal imaging strategy can be developed for FDOT if we conduct larger scaled studies based on more sophisticated modeling techniques that include more acquisition parameters.

Acknowledgment

This study was funded by NIH/NCRR P41 RR005959 and NCI SAIRP U24 CA092656. The authors are grateful to Professor G. Allan Johnson for his mentorship and to Sally Zimney for her assistance in editing.

References and links

1. Wessels JT, Busse AC, Mahrt J, Dullin C, Grabbe E, Mueller GA. In vivo imaging in experimental preclinical tumor research--a review. Cytometry A 2007;71:542–549. [PubMed: 17598185]
2. Ntziachristos V, Ripoll J, Wang LV, Weissleder R. Looking and listening to light: the evolution of whole-body photonic imaging. Nat. Biotechnol 2005;23:313–320. [PubMed: 15765087]
3. Grimm J, Kirsch DG, Windsor SD, Kim CF, Santiago PM, Ntziachristos V, Jacks T, Weissleder R. Use of gene expression profiling to direct in vivo molecular imaging of lung cancer. Proc Natl. Acad. Sci. U S A 2005;102:14404–14409. [PubMed: 16183744]
4. Patwardhan S, Bloch S, Achilefu S, Culver J. Time-dependent whole-body fluorescence tomography of probe bio-distributions in mice. Opt. Express 2005;13:2564–2577.
5. Cherry SR. In vivo molecular and genomic imaging: new challenges for imaging physics. Phys. Med. Biol 2004;49:R13–R48. [PubMed: 15012005]

6. Herve L, Koenig A, Da Silva A, Berger M, Boutet J, Dinten JM, Peltie P, Rizo P. Noncontact fluorescence diffuse optical tomography of heterogeneous media. Appl. Opt 2007;46:4896–4906. [PubMed: 17676093]
7. Patwardhan SV, Culver JP. Quantitative diffuse optical tomography for small animals using an ultrafast gated image intensifier. J. Biomed. Opt 2008;13:011009. [PubMed: 18315358]
8. Lin Y, Gao H, Nalcioglu O, Gulsen G. Fluorescence diffuse optical tomography with functional and anatomical a priori information: feasibility study. Phys. Med. Biol 2007;52:5569–5585. [PubMed: 17804882]
9. Meyer H, Garofalakis A, Zacharakis G, Psycharakis S, Mamalaki C, Kioussis D, Economou EN, Ntziachristos V, Ripoll J. Noncontact optical imaging in mice with full angular coverage and automatic surface extraction. Appl. Opt 2007;46:3617–3627. [PubMed: 17514324]
10. Ntziachristos V, Weissleder R. Experimental three-dimensional fluorescence reconstruction of diffuse media by use of a normalized Born approximation. Opt. Lett 2001;26:893–895. [PubMed: 18040483]
11. Turner G, Zacharakis G, Soubret A, Ripoll J, Ntziachristos V. Complete-angle projection diffuse optical tomography by use of early photons. Opt. Lett 2005;30:409–411. [PubMed: 15762444]
12. Milstein AB, Stott JJ, Oh S, Boas DA, Millane RP, Bouman CA, Webb KJ. Fluorescence optical diffusion tomography using multiple-frequency data. J. Opt. Soc. Am. A Opt. Image Sci. Vis 2004;21:1035–1049. [PubMed: 15191186]
13. Gibson AP, Hebden JC, Arridge SR. Recent advances in diffuse optical imaging. Phys. Med. Biol 2005;50:R1–R43. [PubMed: 15773619]
14. Jorge R, Vasilis N. Imaging scattering media from a distance: theory and applications of noncontact optical tomogarphy. Modern Physics Letters, B 2004;18:1403–1431.
15. Ntziachristos V, Tung CH, Bremer C, Weissleder R. Fluorescence molecular tomography resolves protease activity in vivo. Nat. Med 2002;8:757–760. [PubMed: 12091907]
16. Schulz RB, Ripoll J, Ntziachristos V. Noncontact optical tomography of turbid media. Opt. Lett 2003;28:1701–1703. [PubMed: 13677542]
17. Kepshire DS, Davis SC, Dehghani H, Paulsen KD, Pogue BW. Subsurface diffuse optical tomography can localize absorber and fluorescent objects but recovered image sensitivity is nonlinear with depth. Appl. Opt 2007;46:1669–1678. [PubMed: 17356609]
18. Schulz RB, Peter J, Semmler W, D'Andrea C, Valentini G, Cubeddu R. Comparison of noncontact and fiber-based fluorescence-mediated tomography. Opt. Lett 2006;31:769–771. [PubMed: 16544618]
19. Deliolanis N, Lasser T, Hyde D, Soubret A, Ripoll J, Ntziachristos V. Free-space fluorescence molecular tomography utilizing 360 degrees geometry projections. Opt. Lett 2007;32:382–384. [PubMed: 17356660]
20. Bloch S, Lesage F, McIntosh L, Gandjbakhche A, Liang K, Achilefu S. Whole-body fluorescence lifetime imaging of a tumor-targeted near-infrared molecular probe in mice. J. Biomed. Opt 2005;10:054003. [PubMed: 16292963]
21. Pogue BW, McBride TO, Osterberg UL, Paulsen KD. Comparison of imaging geometries for diffuse optical tomography of tissue. Optics Express 1999;4:270–286. [PubMed: 19396284]
22. Culver JP, Ntziachristos V, Holboke MJ, Yodh AG. Optimization of optode arrangements for diffuse optical tomography: A singular-value analysis. Opt. Lett 2001;26:701–703. [PubMed: 18040425]
23. Sun J, Fu K, Wang A, Lin AW, Utzinger U, Drezek R. Influence of fiber optic probe geometry on the applicability of inverse models of tissue reflectance spectroscopy: computational models and experimental measurements. Appl. Opt 2006;45:8152–8162. [PubMed: 17068558]
24. Boas DA, Dale AM, Franceschini MA. Diffuse optical imaging of brain activation: approaches to optimizing image sensitivity, resolution, and accuracy. Neuroimage 2004;23:S275–S288. [PubMed: 15501097]
25. Xu H, Dehghani H, Pogue BW, Springett R, Paulsen KD, Dunn JF. Near-infrared imaging in the small animal brain: optimization of fiber positions. J. Biomed. Opt 2003;8:102–110. [PubMed: 12542386]

26. Toronov V, D'Amico E, Hueber D, Gratton E, Barbieri B, Webb A. Optimization of the signal-to-noise ratio of frequency-domain instrumentation for nearinfrared spectro-imaging of the human brain. Optics Express 2003;11:2717–2729.
27. Lasser T, Ntziachristos V. Optimization of 360 projection fluorescence molecular tomography. Medical Image Analysis 2007;11:389–399. [PubMed: 17524701]
28. Zhang X, Toronov V, Webb AG. Simultaneous integrated diffuse optical tomography and functional magnetic resonance imaging of the human brain. Optics Express 2005;13:5513–5521.
29. Schulz, R.; Joerg, P.; Wolfhard, S.; Cosimo, D.; Gianluca, V.; Rinaldo, C. Quantifiability and image quality in noncontact fluorescence tomography. In: Kai, L.; Rinaldo, C., editors. SPIE. 2005. p. 58590Z
30. Fletcher R, Reeves CM. Function minimization by conjugate gradients. The Computer Journal 1964;7:149–154.
31. Nakayama A, Bianco AC, Zhang CY, Lowell BB, Frangioni JV. Quantitation of brown adipose tissue perfusion in transgenic mice using near-infrared fluorescence imaging. Mol. Imaging 2003;2:37–49. [PubMed: 12926236]
32. Jacob M, Bresler Y, Toronov V, Zhang X, Webb A. Level-set algorithm for the reconstruction of functional activation in near-infrared spectroscopic imaging. J. Biomed. Opt 2006;11:064029. [PubMed: 17212552]
33. Pogue BW, McBride TO, Prewitt J, Osterberg UL, Paulsen KD. Spatially variant regularization improves diffuse optical tomography. Appl. Opt 1999;38:2950–2961. [PubMed: 18319877]
34. Graves EE, Culver JP, Ripoll J, Weissleder R, Ntziachristos V. Singular-value analysis and optimization of experimental parameters in fluorescence molecular tomography. J. Opt. Soc. Am. A Opt. Image Sci. Vis 2004;21:231–241. [PubMed: 14763766]

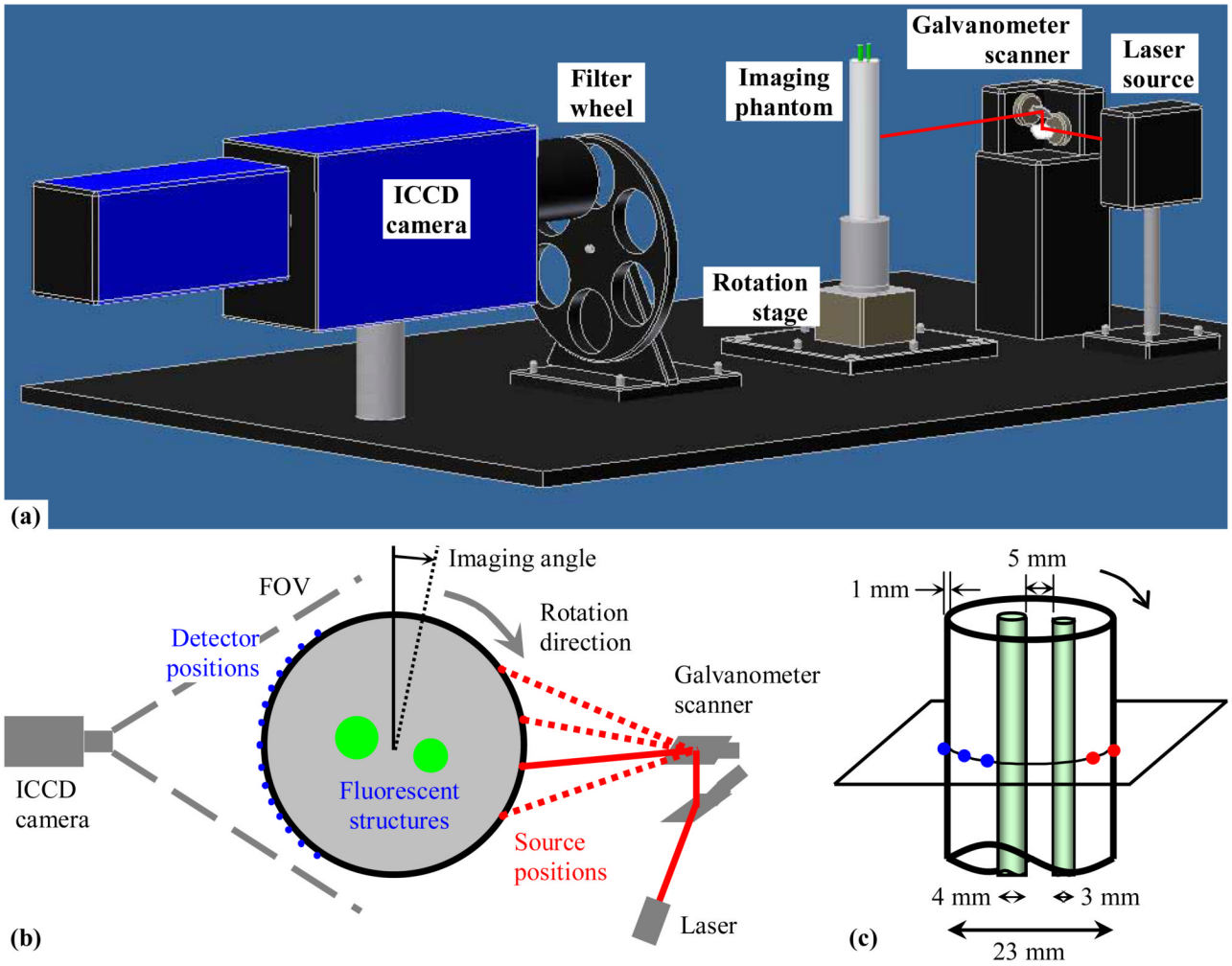

Fig. 1.
Schematics of (a) the FDOT system setup, (b) experimental configuration and sampling strategy, and (c) geometry of the imaging phantom.

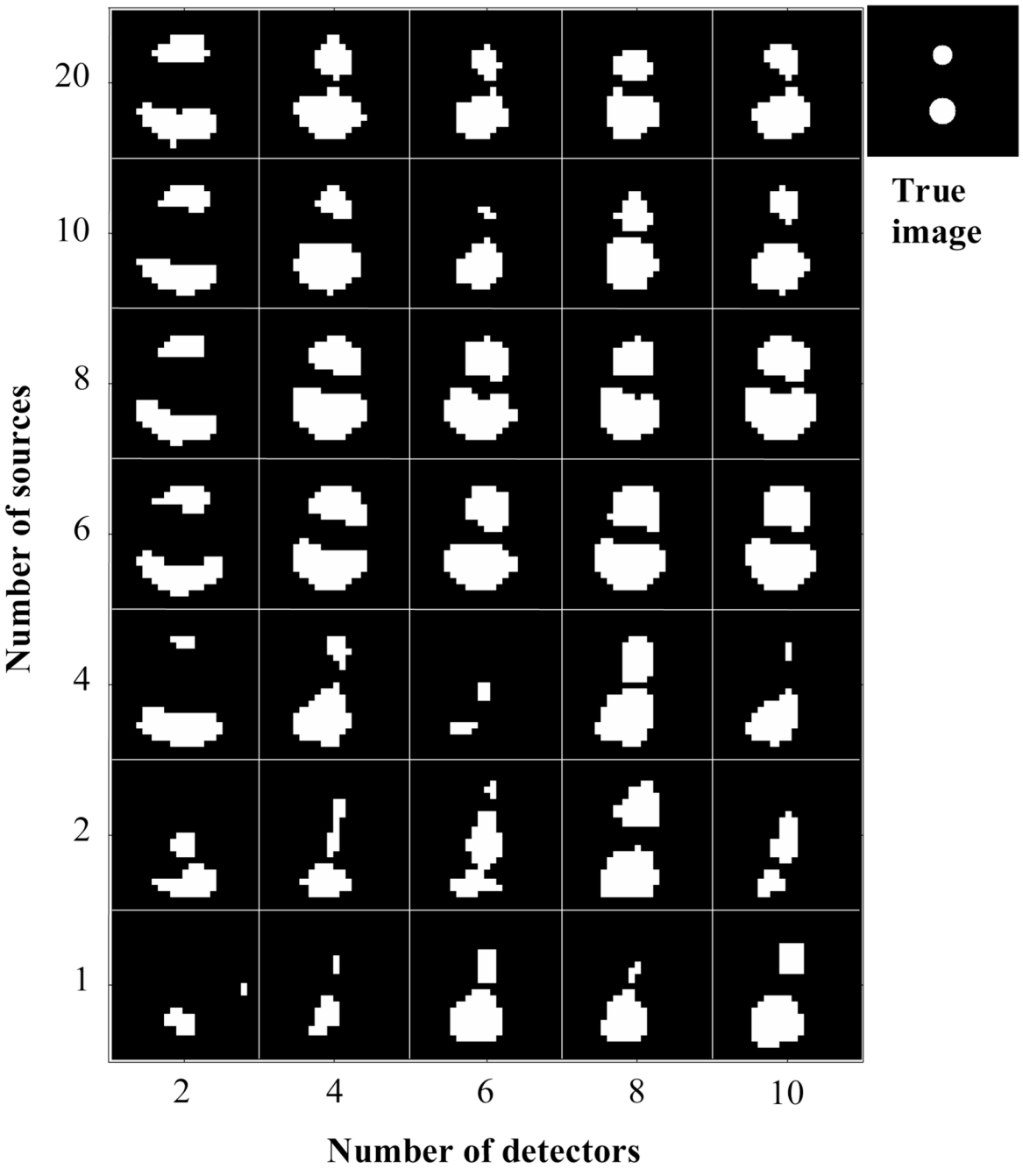

Fig. 2.
Comparison of reconstructed images (23×23 pixels FOV with 1 mm/pixel) using different numbers of sources and detectors (fixed 16 imaging angles). In the true image, the upper area is the smaller fluorescent structure (3 mm diameter); and the lower one is the larger structure (4 mm).

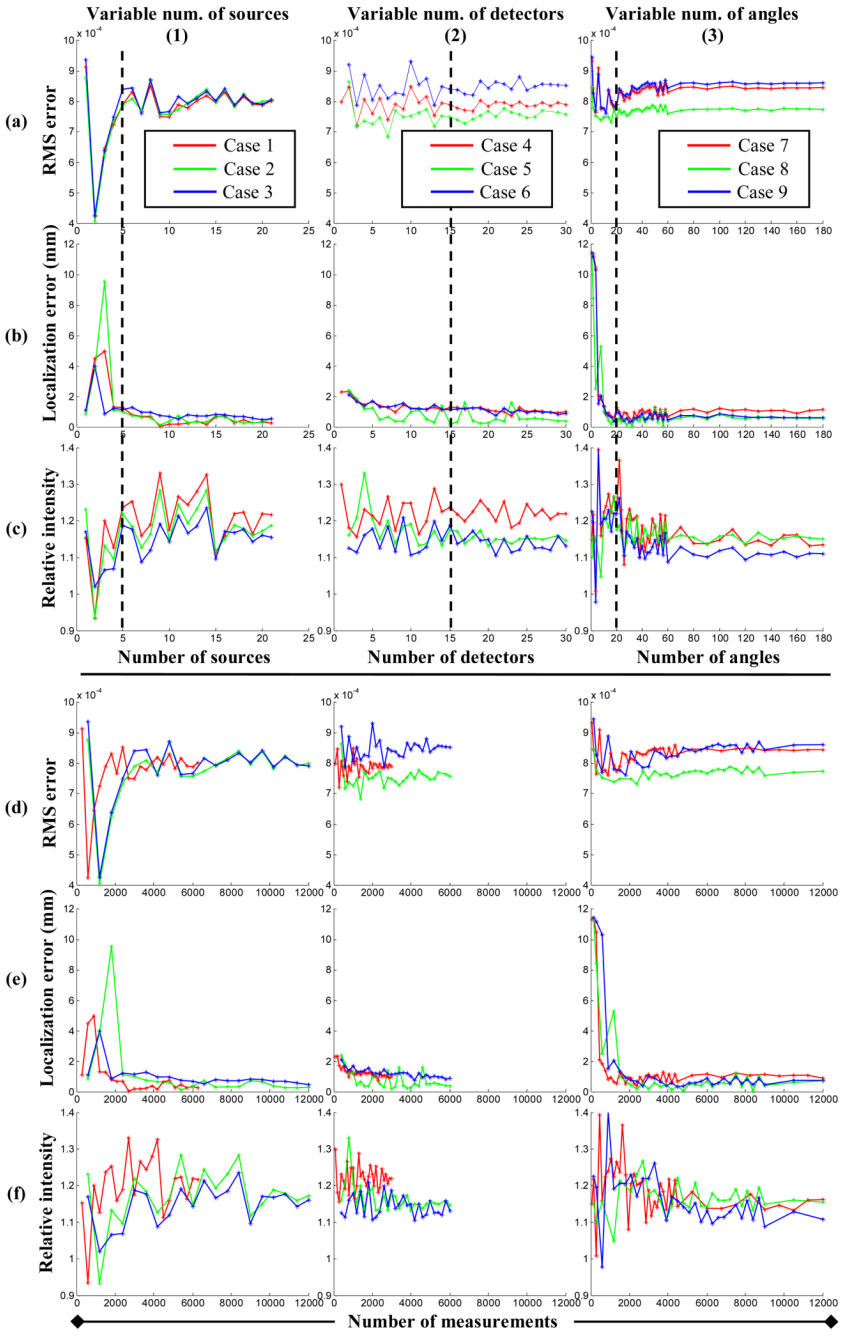

Fig. 3.

Image quality metrics derived from experimental data in terms of (a) RMS error, (b) localization error, and (c) relative intensity in different study cases, from left to right: variable number of sources (Cases 1 to 3), detectors (Cases 4 to 6), and imaging angles (Cases 7 to 9). The bottom rows (d–f) are derived from the same data as in (a–c) but are plotted against the number of measurements.

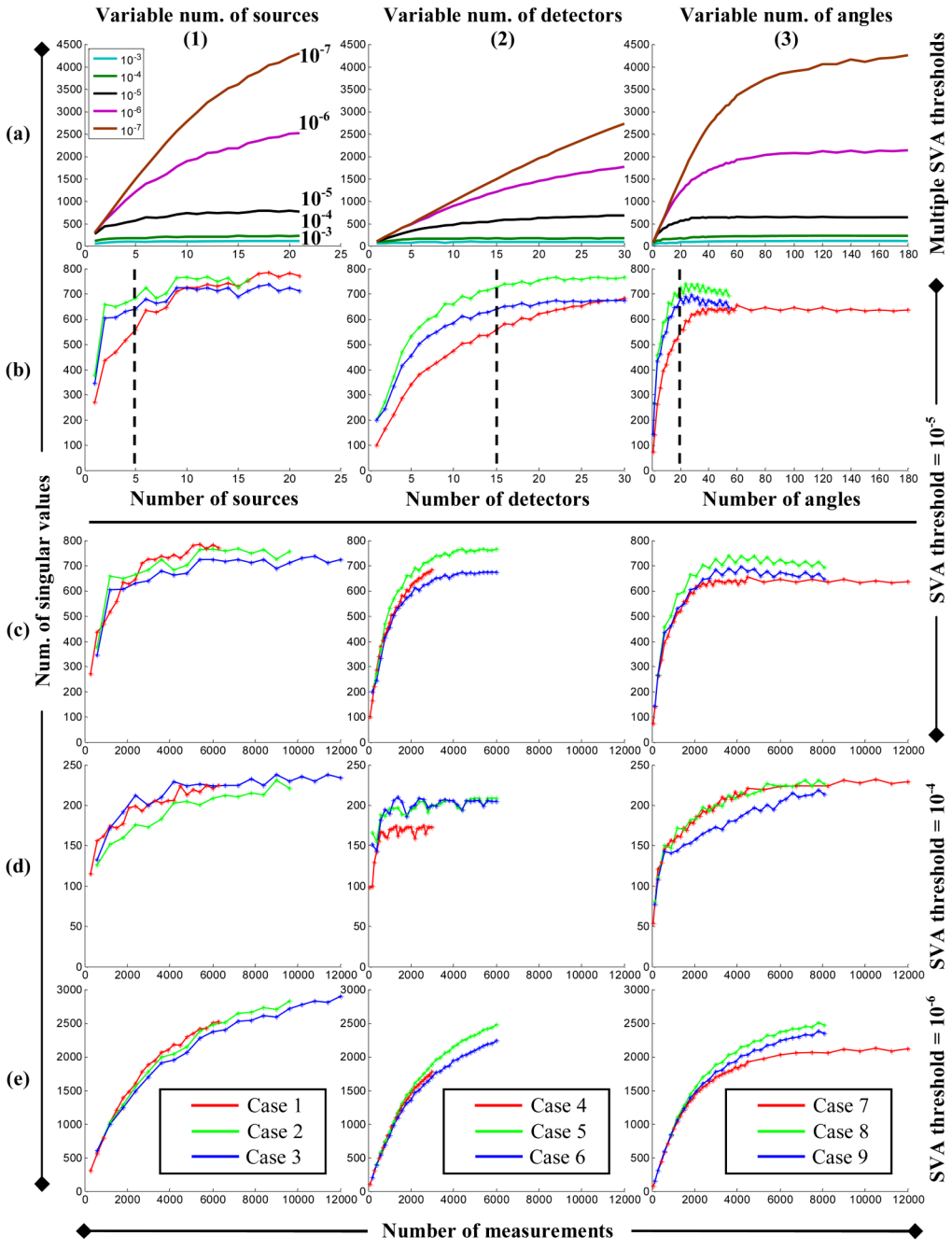

Fig. 4.

(a) and (b) Comparison of the NSV against variable acquisition parameters and (c)–(e) the number of measurements using different thresholds in SVA in each of the study cases, from left to right: variable number of sources (Cases 1 to 3), number of detectors (Cases 4 to 6), and number of angles (Cases 7 to 9). All of the vertical axes represent the NSV, although their scales are different among different rows. The horizontal axes in (a) and (b) are the number of source, the number of detectors, and the number of angles (left to right, respectively); and those in (c)–(e) are the number of measurements.

Table 1

Optical properties of the imaging phantom at 785 nm.

Component	Intralipid-ink	Nylon 6/6
Absorption coefficient μ_a (1/cm)	0.1	<0.001
Reduced scattering coefficient μ'_s (1/cm)	10	3.9
Index of refraction n	1.4	1.5

Table 2

Sampling strategies used in experiment (*var* are variable acquisition parameters.)

Case	**#1**	**#2**	**#3**	**#4**	**#5**	**#6**	**#7**	**#8**	**#9**
Number of sources	*var*	*var*	*var*	5	10	5	5	10	5
Number of detectors	15	30	15	*var*	*var*	*var*	15	15	30
Number of angles	20	20	40	20	20	40	*var*	*var*	*var*